**NON-PEER REVIEWED PREPRINT**
Submitted to EarthArXiv

Also submitted to: *Planetary Science Journal* (AAS), manuscript #AAS77321, 27 May 2026

This preprint has not been peer reviewed.

---

# Lunar Formation by Triple Phase Transition in the Differentiating Proto-Earth

Michel Debailleul

Université libre de Bruxelles (ULB)
1000 Brussels, Belgium

ORCID: 0009-0003-1222-1433

michel.debailleul@yahoo.fr

28 May 2026

---

**Preprint DOI:** https://doi.org/10.5281/zenodo.20367218

**OSF project:** https://doi.org/10.17605/OSF.IO/5DACG

**Interactive simulation:**
https://orion4622.github.io/moon-formation-triple-phase-transition/Animation_Formation_de_la_Lune_v2.html

# Lunar Formation by Triple Phase Transition

# in the Differentiating Proto-Earth

Michel Debailleul

Université libre de Bruxelles (ULB)
1000 Brussels, Belgium
ORCID: 0009-0003-1222-1433
michel.debailleul@yahoo.fr

2026

*Submitted to the Planetary Science Journal (AAS), manuscript #AAS77321.*
*Pre-registered predictions: https://doi.org/10.5281/zenodo.20367219*
*Interactive simulation: https://orion4622.github.io/moon-formation-triple-phase-transition/*

# Abstract

The origin of the Moon remains one of the open questions of planetary science. The canonical giant impact model (Theia collision) predicts neither the near-isotopic identity of Earth and Moon, nor the crustal dichotomy, nor the $\approx 300$ Myr delay of the terrestrial dynamo. The synestia model faces similar limitations. This work proposes a conceptually distinct alternative — an entirely internal mechanism requiring no external impactor and no synestia — grounded in a necessary thermodynamic observation: any Earth-mass planet emerges from accretion in a state of near-total melting ($E_{\text{grav}}$ exceeds the mantle fusion energy by a factor of 155). The proto-Earth is therefore necessarily a rapidly rotating magma sphere ($T_{\text{rot}} \approx 5$ h), without a stabilizing satellite, evolving in a permanently out-of-equilibrium Hadean environment — silicate atmosphere at 2 000–4 000 K, T-Tauri Sun, active residual bombardment — for 30 to 50 million years.
In this context, Moon formation results from a **Triple Phase Transition** driven by the progressive segregation of Fe-Ni. The chaotic wobble of the rotation axis in the co-rotating body frame — sustained by continuous Hadean perturbations — generates toroidal flows that enter elliptical parametric resonance with the inertial modes of the fluid [Malkus, 1968, Kerswell, 2002, Lacaze et al., 2004]. The resulting growth rate $\sigma_{\text{res}} = \Omega f/2$ (linear regime) brings the Coherent Magmatic Torus (TMC) to the bifurcation velocity $U_{\text{crit}} \approx 9.8\,\text{km s}^{-1}$ in $\approx 32$ hours. Three coupled transitions produce $N = 2$–$3$ cohesive ejection episodes in 3–4 weeks and a Hadean dynamo delay of 290–360 Myr [Tarduno et al., 2015, 2025]. The model formulates ten quantitative and falsifiable predictions. The central prediction — seismic interface at $d \approx 200$–$315$ km, impedance contrast $|R| \in [0.01; 0.04]$ — is testable by Chang'e 7, a mission designed to probe lunar internal structure with a broadband seismometer at the lunar south pole (August 2026). The geochemical predictions are testable by Artemis III (2028–2029), a mission that will collect mantle materials from the South Pole-Aitken basin — the deepest and oldest impact structure on the Moon. This deposit pre-registers the theory and its predictions prior to these mission data.

**Keywords:** lunar origin · Triple Phase Transition · elliptical parametric resonance · Hadean proto-Earth · Maclaurin spheroid · Fe-Ni segregation · Coherent Magmatic Torus · seismic interface · crustal dichotomy · Hadean dynamo · Chang'e 7 · Artemis III · falsifiable predictions

# Contents

Chapter 1

# The Hadean Context: Initial Conditions and Thermal Environment of the Proto-Earth

Any theory of lunar formation rests on initial conditions. Before describing the mechanisms, the state of the proto-Earth must be rigorously established — not as working hypotheses, but as necessary consequences of planetary accretion.

## 1.1 The Proto-Earth as the Product of Prior Accretion

**H0 — Initial State of the Proto-Earth.** At $t = 0$, the silicate mantle is in near-total melt. Fe-Ni is dissolved in the molten silicate; no differentiated core exists. This state results from accretionary history: the gravitational energy released exceeds the total mantle fusion energy by a factor of 155 [Solomatov, 2000, Elkins-Tanton, 2012, Rubie et al., 2015].
From this accretionary history follow, without additional postulate, the four initial conditions of the Triple Phase Transition.

**Total melting.** The gravitational energy released during terrestrial accretion [Safronov, 1969]:

$$E_{\text{grav}} = \frac{3\,G\,M_{\oplus}^2}{5\,R_{\text{eq,proto}}} \approx 2.49 \times 10^{32}\,\text{J} \tag{1.1}$$

exceeds the energy required to melt the entire silicate mantle by a factor of 155 [Solomatov, 2000, Elkins-Tanton, 2012]. Total melting is a thermodynamic inevitability of accretion, not an ad hoc hypothesis.

**Rapid rotation.** Conservation of the total angular momentum of the Earth-Moon system ($L_{\text{total}} \approx 3.46 \times 10^{34}\,\text{J s}$) and the moment of inertia factor of the undifferentiated body ($k_{\text{proto}} \approx 0.378$) give:

$$T_{\text{rot}}^{(0)} = \frac{2\pi\,I_{\text{proto}}}{L_{\text{spin}}^{(0)}} \approx \mathbf{5}\,\text{h}. \tag{1.2}$$

This value is the median of N-body accretion simulations [Agnor et al., 1999, Kokubo & Genda, 2010]; it is inherited from collisional history.

**Rehomogenized Fe-Ni.** The last giant impacts between planetary embryos systematically rehomogenized the mantle. The Fe-Ni segregation driving the Triple Phase Transition therefore restarts from an initially homogeneous state.

**Chaotic obliquity in the body frame.** In the absence of a stabilizing satellite, the angle $\varepsilon$ between the rotation vector $\boldsymbol{\Omega}$ and the principal inertia axis of the Maclaurin spheroid — defined in the **co-rotating body frame** — evolves chaotically within $[40°, 70°]$ [Laskar et al., 1993a, Laskar & Robutel, 1993b, Touma & Wisdom, 1993]. This misalignment is sustained by continuous Hadean perturbations (Chapter 3).

## 1.2 Proto-Earth Radius: $R_{\text{eq,proto}} \approx 7.4\,\mathbf{Mm}$

The equatorial radius of the Maclaurin spheroid of the undifferentiated proto-Earth is $R_{\text{eq,proto}} \approx 7.4\,\text{Mm}$ (versus the current $R_\oplus = 6.371\,\text{Mm}$). Three independent physical effects combine: reduced density (unsegregated Fe-Ni, $\rho \approx 4\,900\,\text{kg m}^{-3}$, $+4.0\,\%$), thermal expansion (magma at 3 000–4 000 K, $+7.5\,\%$), and equatorial bulge ($f \approx 0.107$, $+7.5\,\%$), for a total of $+19\,\%$. This correction directly affects the equatorial effective gravity ($g_{\text{eff}}^{(0)} \approx 6.42\,\text{m s}^{-2}$) and the bifurcation velocity ($U_{\text{crit}} \approx 9.79\,\text{km s}^{-1}$), and is used throughout all equations of the model.

## 1.3 An Extreme Thermal and Radiative Environment

The proto-Earth does not evolve in isolation. A dense silicate atmosphere (2 000–4 000 K) acts as a thermal lid: its high infrared opacity reduces surface radiative cooling by a factor of $10^4$ to $10^5$, maintaining the TPT active window for 30 to 50 million years.

The T-Tauri Sun — extreme X and UV radiation, dense stellar winds, coronal mass ejections (CMEs) up to $10^{26}$ J — prevents hydrodynamic escape of this atmosphere [Feigelson & Montmerle, 1999, Airapetian et al., 2016]. CMEs and residual planetesimal bombardment constitute energetic perturbations that contribute to maintaining the chaotic obliquity and to triggering mechanical instability episodes (Chapter 3).

## Chapter 2

# Maclaurin Geometry and the Body Frame

The equilibrium shape of a rotating fluid body is a Maclaurin spheroid [Chandrasekhar, 1969]. At $T_{\rm rot} = 5\,\mathrm{h}$, this spheroid has a flattening $f \approx 0.107$ and an equatorial bulge of $\approx 762\,\mathrm{km}$. This geometry determines the distribution of effective gravity, the preferred location of the TMC, and the conditions for tangential ejection.

The effective gravity at latitude $\varphi$ in the body frame is:

$$g_{\rm eff}(\varphi) = g_{\rm eff}^{(0)}\left(1 + \tfrac{3}{2} f \sin^2\varphi\right) - \Omega^2\, r(\varphi)\cos^2\varphi, \quad r(\varphi) = R_{\rm eq,proto}(1 - f\sin^2\varphi). \tag{2.1}$$

It is minimal in the band $|\varphi| < 30°$. Material in the TMC is ejected **tangentially** in the plane of the spheroid; the tangential component of gravity to be overcome is:

$$g_{\rm tang}(\varphi) = g_{\rm eff}(\varphi) \cdot f \cdot \sin(2\varphi) \in [0.11\,;\,0.65]\,\mathrm{m\,s^{-2}} \quad \text{for } \varphi \in [5°, 30°], \tag{2.2}$$

ten to eighty times smaller than vertical $g_{\rm eff}$.

**Definition of $\varepsilon$ in the TPT model.** $\varepsilon \in [40°, 70°]$ is the instantaneous angle between $\boldsymbol{\Omega}$ and the principal inertia axis of the Maclaurin spheroid, defined entirely within the **co-rotating body frame**. All forces, projections and equations in this work are expressed in this frame. This obliquity range results from the chaotic dynamics of a rapidly rotating body without a stabilizing satellite [Laskar et al., 1993a, Laskar & Robutel, 1993b, Touma & Wisdom, 1993], and is maintained by continuous Hadean perturbations (Chapter 3).

The free (Euler) nutation period is:

$$\omega_{\rm E} = \Omega f \approx 3.74 \times 10^{-5}\,\mathrm{rad\,s^{-1}}, \quad T_{\rm nut} \approx 46.7\,\mathrm{h}. \tag{2.3}$$

Chapter 3

# Maintenance of Obliquity in the Out-of-Equilibrium Hadean Context

An isolated rotating fluid body tends, over the long term, to align its rotation axis with its principal inertia axis. The Hadean proto-Earth satisfies none of the conditions required to apply this result: it is not isolated, not near equilibrium, not weakly perturbed, and not of simple Newtonian rheology.

## 3.1 The Hadean System is Permanently Forced

The relaxation time toward alignment for a viscous planetary-size body can be estimated as:

$$\tau_{\text{relax}} \sim \frac{\eta\, R_{\text{eq,proto}}^3}{G\, M_\oplus^2\, f} \approx 10^6\,\text{yr} \quad (\eta \sim 10^{1\text{–}3}\,\text{Pa s},\ f \approx 0.107). \tag{3.1}$$

This timescale must be compared to the timescales of the perturbations that continuously push the system away from alignment:

| **Perturbation** | **Timescale** |
|---|---|
| T-Tauri eruptions (CMEs) | Days to weeks |
| Residual planetesimal impacts | $10^3$–$10^5$ yr |
| Extreme thermal convection ($\Delta T \sim 2\,000\,\text{K}$) | Continuous, $\sim 10^3$ yr |
| Ongoing Fe-Ni differentiation | $\tau_{\text{seg}} \approx 40\,\text{Myr}$ |
| Inertia tensor reorganization | Continuous |

Each of these perturbations modifies the inertia tensor or imprints a variation of $\boldsymbol{\Omega}$ on timescales well below $\tau_{\text{relax}}$. The system is pushed away from alignment before it can reach it.

## 3.2 Bingham Rheology Further Sustains the Misalignment

The Bingham-Herschel law introduces a yield stress $\tau_y \in [10^2, 10^4]$ Pa. Below this threshold, the fluid behaves as a solid: the inertia tensor cannot freely readjust instantaneously. The rheological response time to a stress perturbation is of order:

$$\tau_{\text{BH}} \sim \frac{\tau_y}{\mu\,\dot{\gamma}_{\text{typ}}} \approx 10^2\text{–}10^4\,\text{s}, \tag{3.2}$$

which locally freezes mass redistribution and further slows relaxation toward alignment.

**Conclusion.** The misalignment $\varepsilon \in [40^\circ, 70^\circ]$ is sustained not by an intrinsic property of the fluid, but by the permanent imbalance between the relaxation time ($\tau_{\text{relax}} \sim 10^6$ yr) and the timescales of continuous perturbations (days to $10^5$ yr). This forced regime is the normal condition of a Hadean proto-Earth.

Chapter 4

# Precession Flows and Elliptical Parametric Resonance

## 4.1 Precession Flows — Poincaré (1910)

The wobble of the proto-Earth in the body frame implies $\dot{\boldsymbol{\Omega}} \neq \mathbf{0}$. Poincaré (1910) showed that this variation exerts on each fluid particle an Euler acceleration [Poincaré, 1910, Noir & Cébron, 2013]:

$$\boldsymbol{a}_{\text{Euler}} = \dot{\boldsymbol{\Omega}} \times \boldsymbol{r}. \tag{4.1}$$

This acceleration generates a large-scale toroidal flow concentrated in the Hadean intertropical band $|\varphi| < 30°$ where $|\boldsymbol{r}|$ is maximal. This band is defined entirely in the co-rotating body frame, perpendicular to the instantaneous rotation axis $\boldsymbol{\Omega}$ — not to the geographic equator. Since $\varepsilon \in [40°, 70°]$, it wobbles with the body frame at the nutation period $T_{\text{nut}} \approx 47\,\text{h}$, sweeping all geographic latitudes over the course of one episode. Its geometry is identical to that of the TMC: the coupling between precession forcing and the toroidal mode is direct.

## 4.2 Elliptical Parametric Instability

In a fluid ellipsoid subject to precession, the precession flows can enter resonance with the fluid's own inertial modes (Poincaré waves, frequencies $\omega_{\text{in}} = 2\Omega m/n$). This mechanism — elliptical parametric instability — was established theoretically by Malkus [1968], formalized by Kerswell [2002], and demonstrated experimentally by Lacaze et al. [2004].

**The resonance condition is satisfied by Maclaurin geometry.** At $T_{\text{rot}} = 5\,\text{h}$ and $f = 0.107$, the free nutation frequency is $\omega_{\text{E}} = \Omega f \approx 3.74 \times 10^{-5}\,\text{rad}\,\text{s}^{-1}$. This frequency is commensurate with the fluid inertial modes by geometric construction — not by adjustment of a free parameter. The linear growth rate of the instability is [Kerswell, 2002, Lacaze et al., 2004]:

$$\boxed{\sigma_{\text{res}} = \frac{\Omega f}{2} \approx 1.87 \times 10^{-5}\,\text{rad}\,\text{s}^{-1}.} \tag{4.2}$$

### 4.2.1 External Forcings

While internal precession is sufficient to sustain the resonance, several external forcings lower the effective bifurcation threshold: T-Tauri coronal eruptions ($10^{25}$–$10^{26}$ J) [Feigelson & Montmerle, 1999], residual planetesimal bombardment, solar and giant-planet tidal forcing during migration, stellar wind interaction with the silicate atmosphere.

### 4.2.2 Dissipation and Resonance Survival

For the resonance to survive, $\sigma_{\text{res}}$ must exceed the dissipation rates. In Bingham magma, viscous dissipation gives $\nu k^2$ with $\nu \sim 10^{-6}\,\text{m}^2\,\text{s}^{-1}$; nonlinear dissipation linked to the yield stress $\tau_y$ is of order $\tau_y/(\rho U \delta)$. For typical values ($\tau_y \sim 10^2$–$10^3$ Pa, $U \sim$ km s$^{-1}$, $\delta \sim$ km), one obtains $\sigma_{\text{res}} \gg$ dissipation rates.

## 4.3 TMC Growth and Lightening by Fe-Ni Segregation

The TMC velocity grows exponentially:

$$U_{\text{TMC}}(t) = U_{\text{Rhines}}\, e^{\sigma_{\text{res}} t}, \qquad U_{\text{Rhines}} \approx 0.8\,\text{km}\,\text{s}^{-1}, \tag{4.3}$$

where $U_{\text{Rhines}}$ is the characteristic velocity of flows at the Rhines scale [Rhines, 1975]. The time to reach $U_{\text{crit}} \approx 9.8\,\text{km}\,\text{s}^{-1}$ is:

$$t_{\text{acc}} = \frac{\ln(U_{\text{crit}}/U_{\text{Rhines}})}{\sigma_{\text{res}}} \approx 32\,\text{h}. \tag{4.4}$$

This result is entirely determined by $f = 0.107$ and $\Omega = 3.491 \times 10^{-4}\,\text{rad}\,\text{s}^{-1}$, imposed by $T_{\text{rot}} = 5\,\text{h}$ and the physics of the Maclaurin spheroid.
As Fe-Ni segregates, the TMC density decreases:

$$\rho_{\text{TMC}}(t) = \rho_0 - \xi_{\text{Fe}}(t)(\rho_0 - \rho_f), \quad \rho_0 \approx 4\,500\,\text{kg}\,\text{m}^{-3},\ \rho_f \approx 3\,200\,\text{kg}\,\text{m}^{-3}, \tag{4.5}$$

amplifying all destabilizing terms via the factor $\rho_0/\rho_{\text{TMC}}(t)$ in the instability equation.

## Chapter 5

# The Generalized Instability Equation

The radial equation of motion of a TMC fluid particle in the co-rotating body frame, projected onto the local normal to the Maclaurin spheroid, gives:

$$\lambda_{\text{global}}(\varphi,\varepsilon,t) = \Bigg[\underbrace{-\frac{g_{\text{eff}}(\varphi)}{R_{\text{eq,proto}}}}_{\lambda_1<0} + \underbrace{\frac{2\Omega\sin\varepsilon\cos\varphi\cdot U}{R_{\text{eq,proto}}}}_{\lambda_2\ \text{[Coriolis]}} + \underbrace{\frac{(\alpha-1)U^2}{R_{\text{eq,proto}}^2}}_{\lambda_3\ \text{[rotation]}} + \underbrace{\frac{|\dot{\Omega}|\,r(\varphi)\sin(\varepsilon+\varphi)}{R_{\text{eq,proto}}}}_{\lambda_4\ \text{[precession]}} + \underbrace{\frac{g_{\text{eff}}^{(0)} f\sin(2\varphi)}{R_{\text{eq,proto}}}}_{\lambda_5\ \text{[Maclaurin]}}\Bigg]\cdot\frac{\rho_0}{\rho_{\text{TMC}}(t)} \tag{5.1}$$

Term $\lambda_1$ is the local effective gravity, opposing ejection. Term $\lambda_2$ is the generalized radial Coriolis force at all latitudes; the $\cos\varphi$ factor extends the original term from the Hadean intertropical band to the entire body-frame surface. Term $\lambda_3$ accounts for the angular momentum gradient associated with the super-rigid rotation profile ($\alpha > 1$). Term $\lambda_4$ quantifies the contribution of precession flows, proportional to $\sin(\varepsilon+\varphi)$. Term $\lambda_5$ represents the tangential effective gravity gradient on the spheroid. The factor $\rho_0/\rho_{\text{TMC}}(t)$ amplifies all destabilizing terms monotonically as the TMC lightens.

**Ejecta are not equatorial.** The wobble of the proto-Earth changes orientation every $\approx 47$ h in the body frame. The band $|\varphi| < 30°$ is the preferred site of instability at each instant, but corresponds to different geographic latitudes at each nutation cycle. Over the duration of one episode, the swept surface covers all body-frame latitudes — which fundamentally distinguishes this model from competing approaches.

Chapter 6

# The Three Coupled Transitions

The driving force of the Triple Phase Transition is unique: the progressive segregation of Fe-Ni toward the forming core. This process orchestrates three closely coupled regime changes.

## 6.1 Transition 1 — Rheological: Bingham-Herschel Law

**Rheological.** As Fe-Ni segregates, the residual silicate magma acquires a yield stress $\tau_y$: the Bingham-Herschel law [Bingham, 1922, Herschel & Bulkley, 1926]. This threshold allows the TMC to accumulate energy from the elliptical resonance without dispersing through turbulence, and to eject as a cohesive mass when the mechanical threshold is crossed.
The Bingham-Herschel law is:

$$\tau = \tau_y + k\,\dot{\gamma}^n \qquad (\tau > \tau_y). \tag{6.1}$$

For a silicate magma at $T = 3\,000$–$3\,500\,\mathrm{K}$ with solid fraction $\phi \approx 0.1$–$0.3$, the yield stress is $\tau_y \in [10^2, 10^4]$ Pa [Giordano et al., 2008, Caricchi et al., 2007]. A natural thermal lock exists at $T^* \approx 1\,800\,\mathrm{K}$: below this temperature, $\tau_y \to 10^6$ Pa and cohesive ejection becomes physically inaccessible. The TPT window therefore closes irreversibly by thermodynamics alone.

## 6.2 Transition 2 — Mechanical: Instability and Ejection

**Mechanical.** When the TMC is brought to bifurcation velocity $U_{\text{crit}}$ by elliptical resonance, the instability coefficient $\lambda_{\text{global}}$ changes sign: the flow spontaneously switches from the confined state to the ejective state. This is a mechanical phase transition, analogous to classical saddle-node bifurcations.
The effective potential of the TMC has a double-well structure (Figure 6.1): ejection episodes are spontaneous transitions between metastable states.

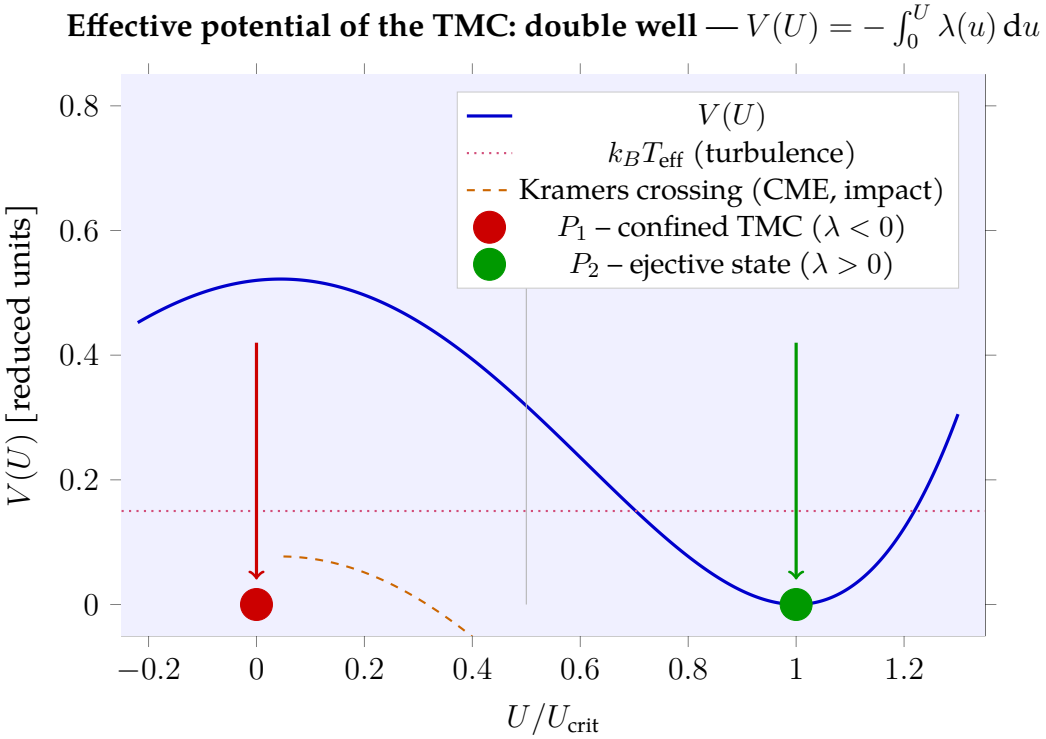


**Figure 6.1:** Effective potential $V(U) = -\int_0^U \lambda(u)\,\mathrm{d}u$ of the Coherent Magmatic Torus. $P_1$ (confined, $\lambda < 0$) and $P_2$ (ejective, $\lambda > 0$) are the two minima, separated by $\Delta E_{\mathrm{barr}}$ (vertical grey line). The dashed orange arc shows the Kramers crossing path triggered by external forcings. The dotted line marks the effective turbulent energy $k_B T_{\mathrm{eff}}$.

### 6.2.1 Maximum Ejectable Mass per Episode

The maximum mass susceptible to ejection per episode is estimated from the force balance in the body frame:

$$\boxed{M_{\mathrm{ej}}^{\max} \approx \frac{2\,\Omega\,\sin\varepsilon \cdot U_{\mathrm{crit}} \cdot M_{\mathrm{TMC}}}{g_{\mathrm{eff}}^{(0)}} \approx 2.0\text{–}3.8 \times 10^{22}\,\mathrm{kg}.} \tag{6.2}$$

The mass $M_{\mathrm{TMC}}$ is not a free parameter: it is constrained by the observed size of the first accretion layer. The proto-lunar body formed by Episode 1 has radius $R_1 \approx 1\,560\,\mathrm{km}$ (Chapter 7), giving:

$$M_{\mathrm{CAO},1} = \frac{4}{3}\pi R_1^3\,\rho_{\mathrm{sil}} \approx 1.6 \times 10^{22}\,\mathrm{kg}, \tag{6.3}$$

and since $M_{\mathrm{CAO},1} = f_{\mathrm{cap}} \cdot M_{\mathrm{TMC}}$:

$$M_{\mathrm{TMC}} \approx \frac{1.6 \times 10^{22}}{0.70} \approx 2.3 \times 10^{22}\,\mathrm{kg}, \tag{6.4}$$

representing $\approx 0.4\,\%$ of the total silicate mantle mass — consistent with a toroidal

structure confined to the Hadean intertropical band $|\varphi| < 30^\circ$ over a radial thickness of $\sim 400$–$600\,\mathrm{km}$.

### 6.2.2 Mass Budget

For $N = 2$–$3$ episodes and a capture factor $f_{\mathrm{cap}} \in [0.5; 0.85]$, the lunar mass is recovered:

$$M_{\mathrm{Moon,TPT}} = N \cdot f_{\mathrm{cap}} \cdot M_{\mathrm{ej}}^{\mathrm{max}} + \Delta M_{\mathrm{late}}. \tag{6.5}$$

The SPA impactor contributes only $0.04\,\%$ of the lunar mass and does not enter this budget.

**On the capture factor $f_{\mathrm{cap}}$.** The value $f_{\mathrm{cap}} = 0.70$ is physically motivated by the geometric coherence of the ejected flux, but is not numerically constrained. Sensitivity analysis over $f_{\mathrm{cap}} \in [0.50; 0.85]$ shows that the mass budget remains consistent throughout this range.

### 6.2.3 Post-Ejection Transient Precession

Each episode instantaneously modifies the inertia tensor ($\Delta\Omega/\Omega \approx -12\,\%$). The new obliquity $\varepsilon'$ remains within $[40^\circ, 70^\circ]$ with high probability ($\approx 70\,\%$) per Touma & Wisdom [1993], allowing $N = 2$–$3$ successive episodes. Beyond this, the system tends to leave the unstable zone, naturally closing the window.

## 6.3 Transition 3 — Magnetic: Delayed Hadean Dynamo

**Magnetic.** The growth of the Fe-Ni core, a direct and delayed consequence of segregation, eventually reaches the threshold of compositional convection required to ignite the terrestrial dynamo.

Core growth modeled as:

$$M_{\mathrm{core}}(t) = M_{\mathrm{core}}^{\infty}\left(1 - e^{-t/\tau_{\mathrm{seg}}}\right), \qquad \tau_{\mathrm{seg}} \approx 40\,\mathrm{Myr}, \tag{6.6}$$

with critical Elsasser number $\Lambda_{\mathrm{Els}}^{\mathrm{crit}} \approx 0.3$, leads to dynamo threshold crossing at $t \approx 330$–$350\,\mathrm{Myr}$.

**Predicted dynamo delay: 290–360 Myr.** This result is consistent with paleomagnetic data from Jack Hills zircons [Tarduno et al., 2015, 2020, 2025].

Chapter 7

# Chronology: Moon Formation in 3–4 Weeks

## 7.1 The Three Phases of an Episode

**Phase 1 — Resonant acceleration.** $\tau_{\text{acc}} = \ln(U_{\text{crit}}/U_{\text{Rhines}})/\sigma_{\text{res}} \approx 1.4$ days.
**Phase 2 — Ejection.** Crossing the Roche radius ($3R_{\text{eq,proto}} \approx 22.2$ Mm) at $U_{\text{crit}}$: $\tau_{\text{ej}} \approx 0.6$ h.
**Phase 3 — Reloading.** The TMC reorganizes over 5–6 nutation periods: $\tau_{\text{rec}} \approx 10$–$12$ days.
The Fe-Ni redistribution within the TMC between episodes follows the Stokes settling law and is quasi-instantaneous ($\tau_{\text{Stokes}} \approx 257$ s; see Appendix D), implying that each accreted layer is chemically distinct from the previous one — a direct consequence of seismic prediction P1.

## 7.2 Two Distinct Fe-Ni Timescales

Two physically distinct processes govern Fe-Ni migration in the TPT framework.
**Global segregation** ($\tau_{\text{seg}} \approx 40$ Myr) describes the large-scale migration of Fe-Ni toward the forming core across the full mantle depth. This defines the slow clock of the TPT window: the system charges over tens of millions of years before the instability threshold is reached.
**Local redistribution within the TMC** ($\tau_{\text{Stokes}} \approx 257$ s) operates under fundamentally different conditions: ultra-rapid rotation, intense shear stress, and a tangential effective gravity ten to eighty times smaller than vertical $g_{\text{eff}}$. Fe-Ni droplets sediment quasi-instantaneously between ejection episodes. Each reloading interval of $\approx 10$–$12$ days is sufficient for complete local chemical re-equilibration.
The apparent paradox between a 3–4 week formation and a 40 Myr segregation timescale is therefore resolved: the slow global clock charges the system; the fast local clock stamps each ejection episode with a distinct chemical signature.

## 7.3 Complete Chronology

1. **Episode 1**: acceleration ($\approx 1.4$ days) + ejection ($\approx 0.6$ h). Proto-CAO formed, $R_1 \approx 1\,560$ km.

2. **Reloading + Episode 2**: $\approx$ 11–13 days. Asymmetric episode: post-ejection transient precession modifies $\varepsilon$, producing the crustal dichotomy (Chapter 8).
3. **Reloading + Episode 3**: $\approx$ 11–13 days. Lunar mass recovered.
4. **Total duration**: $\approx$ 24–28 days.
5. TPT window closes: $t \approx 30$–$50$ Myr.
6. Hadean dynamo ignition: $t \approx 330$–$350$ Myr.

## 7.4 Lunar Age: LMO Solidification versus Formation

The measured age ($4.425 \pm 0.025$ Ga) is that of the solidification of the lunar magma ocean (LMO), not of formation. If the TPT triggers at $\approx 4.467$ Ga, LMO cooling ($\sim 40$ Myr) gives a predicted solidification age:

$$t_{\mathrm{LMO}} \approx 4.467 - 0.040 = 4.427\,\mathrm{Ga}, \tag{7.1}$$

consistent within $0.1\sigma$ with the measured value.

## Chapter 8

# Crustal Dichotomy

GRAIL data [Wieczorek et al., 2013, Zuber et al., 2013] show that the lunar crust is on average 20 km thicker on the far side ($\approx 54$ km) than on the near side ($\approx 34$ km). The Triple Phase Transition produces this asymmetry as a direct mechanical consequence of the second asymmetric episode: post-ejection transient precession modifies the relative orientation of the proto-CAO and the second ejected flux, which accumulates preferentially on one hemisphere. Bingham-Herschel rheology renders this asymmetry irreversible.

The stratigraphic interface between the first two layers lies at:

$$d = R_{\text{Moon}} - R_1 \approx 1\,737 - 1\,560 \approx 177\,\text{km} \quad (N = 2,\ \text{equal masses}), \tag{8.1}$$

and between 200 and 314 km for $N = 3$ — the window of prediction P1.

## Chapter 9

# Falsifiable Predictions

This model formulates ten quantitative and falsifiable predictions, each accompanied by an explicit discussion criterion and an identified validation mission.

**P1 — Seismic interface at $d \approx 200$–$315$ km (Priority 1).** Stratification into $N = 2$–$3$ chemically distinct accretion layers produces a compositional interface whose impedance contrast is estimated at $|R| \in [0.01; 0.04]$, detectable if $|R| > 0.02$ with depth resolution $\leq 30$ km [Garcia et al., 2019]. A discontinuity at $\approx 270$ km is already present in Apollo data [Weber et al., 2011]. Chang'e 7 will test whether it is global.

*Discussion criterion*: absence of phase conversion in the 200–315 km window after $\geq 3$ stations and $\geq 10$ moonquakes $M > 2.5$.

**Mission: Chang'e 7 (south pole, August 2026).**

**P2 — Seismic asymmetry near side / far side.** The asymmetric second episode produces a sharper and deeper interface beneath the far side. *Test*: multi-station network, lunar internal tomography.

**P3 — Fe/Si ratio increasing with depth.** Each episode expels a mantle progressively more depleted in Fe-Ni. The innermost layer (episode 1) is richest in siderophiles. The SPA basin preferentially exposes this material [Schultz & Crawford, 2011, Wakita et al., 2026, Gowman et al., 2026].

**Missions: Chang'e-6 (far side, 2024), Artemis III (SPA ridges, 2028–2029).**

**P3b — Fe enrichment at the lunar south pole: independent observational convergence.** The TPT predicts that Episode 1 ejecta — the oldest and most Fe-rich layer — should be detectable as an elevated Fe/Si ratio where deep excavation has occurred. This prediction finds independent support in existing observations: Lunar Prospector gamma-ray data reveal a broad Fe enhancement across the SPA interior and toward the lunar south pole [Wakita et al., 2026, Gowman et al., 2026]. Simulations of the SPA-forming impact confirm that an oblique southward impactor excavated lower crustal and upper mantle material and redistributed Fe-rich ejecta toward the south pole [Schultz & Crawford, 2011, Wakita et al., 2026]. This convergence is independent: the TPT was not formulated to explain the SPA Fe anomaly. The agreement constitutes a consistency check, not a post-hoc adjustment. Chang'e 7 (2026) will provide high-resolution geochemical mapping; Artemis III (2028–2029) will allow isotopic analysis.

*Discussion criterion*: Fe/Si ratio at the south pole significantly exceeding equatorial Apollo baseline values, with a depth profile consistent with a discontinuity at $d \approx 200$–$315$ km.

**Missions: Chang'e 7 (2026); Artemis III (2028–2029).**

**P4 — Terrestrial dynamo delay: 290–360 Myr.** *Test*: extension of the Jack Hills zircon database [Tarduno et al., 2025].

**P5 — Instability window: $\varepsilon \in [57°, 70°]$ in the body frame.** *Test*: N-body simulations of terrestrial proto-planet obliquity.

**P6 — Polar signature of high-latitude ejecta.** The wobbling proto-Earth ejects from all body-frame latitudes. High-latitude ejecta concentrate preferentially at the lunar south pole during the asymmetric second episode. *Prediction*: elevated Fe/Si ratio and distinct seismic signal at the south pole compared to equatorial Apollo sites.

**Mission: Chang'e 7 (south pole, August 2026).**

**P7 — Hf-W chronometer signature.** A formation duration of 3–4 weeks is the only intermediate time window between the giant impact (hours) and the synestia ($\sim 100$ yr) in the Hf-W chronometer. The $^{182}$Hf/$^{180}$Hf ratio in episode 1 samples must correspond to a differentiation age of $4.467$ Ga ($100 \pm 10$ Myr after CAIs), versus $60 \pm 10$ Myr for the giant impact [Kleine et al., 2002].

**Mission: Artemis III (2028–2029).**

**P8 — Formation age $> 4.45$ Ga.** The measured age of $4.425$ Ga is that of LMO solidification, not formation (Chapter 7). *Test*: direct dating of episode 1 rocks exposed on SPA basin ridges (Artemis III).

**P9 — Compatibility of mare basalts with layer 1.** The estimated melting depth of mare basalts (200–500 km, $\pm 100$ km) is compatible with a source in layer 1 ($> d_{\mathrm{P1}}$). *Test*: high-resolution isotopic geochemistry of Apollo and Chang'e-5 mare basalts [Li et al., 2021].

Chapter 10

# Validation Missions

Three independent space missions will provide data directly comparable to the predictions of this model. Their geographic convergence toward the lunar south pole is not coincidental.

## 10.1 Chang'e 7 — South Pole Seismology (August 2026)

Chang'e 7 (CNSA) will land at the lunar south pole and deploy the first broadband seismometer at this location since Apollo 17 (1972). It directly tests P1 and P6. The prediction is pre-registered and quantified: $d \approx 200$–$315\,\text{km}$, $|R| \in [0.01; 0.04]$.

## 10.2 The South Pole-Aitken Basin: Exhumed Stratigraphy

The SPA impactor is a body external to the proto-Earth system; it does not enter the TPT mass budget. Simulations confirm that an oblique southward impactor excavated lower crustal and upper mantle material and projected Fe-rich ejecta toward the south pole [Schultz & Crawford, 2011, Wakita et al., 2026], making layer 1 materials (episode 1, richest in Fe) accessible without drilling. Gravity mapping further identifies a $\sim 400\,\text{km}$ annulus of mantle-derived material in the SPA rim region [Gowman et al., 2026], consistent with the depth and composition of TPT layer 1.

## 10.3 Artemis III — South Pole Geochemistry (2028–2029)

Artemis III (NASA) will land astronauts near Shackleton crater. Mantle materials concentrated in this zone by the SPA impact [Schultz & Crawford, 2011, Wakita et al., 2026] will allow testing of P3, P3b, P7 and P8 on layer 1 rocks ($> 4.45\,\text{Ga}$).

**Convergence.** Chang'e 7 (2026): P1, P2, P6, P3b. Artemis III (2028): P3, P3b, P7, P8. Two independent agencies, one geographic site, one internal architecture to confirm or refute.

Chapter 11

# Discussion

## 11.1 Position Relative to the Giant Impact Model

A recent review concludes that there is currently no unambiguous geochemical or isotopic evidence for the role of an external impactor in lunar formation [Sossi et al., 2025]. The Triple Phase Transition is an entirely internal mechanism that naturally satisfies isotopic constraints (same mantle source), crustal dichotomy (asymmetric second episode), and the dynamo delay (delayed segregation).

## 11.2 Justification of $\alpha > 1$

Two independent mechanisms lead to a super-rigid rotation profile: differential equator-to-pole cooling generates a density gradient and thermal spin-up; Fe-Ni segregation lightens the TMC, and by angular momentum conservation its inner part accelerates. The Bingham-Herschel yield stress also blocks small scales, favoring a plug-flow profile.

## 11.3 Partial Fragmentation and Coalescence

Even if the ejected sheet partially fragments, fragments remain in the same orbital zone and coalesce rapidly through inelastic collisions and the gravitational attraction of the proto-CAO [Canup & Asphaug, 2001]. The effective capture efficiency therefore remains high ($f_{\text{cap}} \gtrsim 0.7$).

## 11.4 Limitations and Validation Program

The following points are numerically unconstrained and constitute validation priorities:

(**L1**) Spontaneous organization of the TMC in a Bingham-Herschel fluid in ultra-rapid rotation is physically motivated, but not yet demonstrated by simulation. *Priority: SPH 3D simulation, horizon 3–5 years.*

(**L2**) The rate $\sigma_{\text{res}} = \Omega f/2$ is established in the linear regime. The value of $U_{\text{TMC}}$ at nonlinear saturation requires dedicated numerical simulation.

**(L3)** Capture factor $f_{\text{cap}}$ is physically motivated but numerically unconstrained.
**(L4)** Dynamo delay: $\pm 50$ Myr. The core growth model used is simplified.
Validation program, in order of priority: (0) rheological validation in hypersonic regime (1–3 years); (1) seismic data: Chang'e 7, FSS, LEMS, Artemis III (2026–2030); (2) SPH 3D hydrodynamic simulation on oblate sphere at $T_{\text{rot}} = 5$ h (3–5 years); (3) Fe/Si geochemistry, SPA basin; (4) high-precision Hf-W (P7).

## Chapter 12

# Conclusion

This work proposes that Moon formation is the product of a Triple Phase Transition in a fully molten proto-Earth rotating at $\approx 5\,\mathrm{h}$, itself evolving in a permanently out-of-equilibrium Hadean environment. The central mechanism is elliptical parametric resonance: the chaotic wobble of the proto-Earth in the body frame generates toroidal precession flows that resonate with the fluid inertial modes at frequency $\omega_{\mathrm{E}} = \Omega f$. This resonance, satisfied by Maclaurin geometry at $T_{\mathrm{rot}} = 5\,\mathrm{h}$, brings the Coherent Magmatic Torus to bifurcation velocity in $\approx 32\,\mathrm{hours}$.

The unique driving force of Fe-Ni segregation simultaneously orchestrates three coupled transitions — rheological, mechanical, and magnetic — producing $N = 2$–$3$ cohesive ejection episodes in three to four weeks and igniting the Hadean dynamo with a delay of 290–360 Myr.

Original contributions: the identification of elliptical parametric resonance as the TMC acceleration mechanism; a generalized instability equation $\lambda_{\mathrm{global}}(\varphi, \varepsilon, t)$ valid at all body-frame latitudes; a dedicated analysis of obliquity maintenance in the out-of-equilibrium Hadean context; the internal constraint of $M_{\mathrm{TMC}}$ from the observed size of the first accretion layer; a three-to-four-week chronology with ten testable predictions; and the independent observational convergence P3b with existing Lunar Prospector data.

The central prediction stands: seismic interface at $d \approx 200$–$315\,\mathrm{km}$, contrast $|R| \in [0.01; 0.04]$, testable by Chang'e 7 at the lunar south pole in August 2026, and by Artemis III in 2028–2029.

## Appendix A

# Adiabatic Temperature Profile

With a surface temperature $T_{\text{surf}} \approx 3\,500\,\text{K}$ and an adiabatic gradient $\mathrm{d}T/\mathrm{d}r \approx -0.3\,\text{K}\,\text{km}^{-1}$, the central temperature reaches $\approx 5\,000\,\text{K}$. The peridotite solidus at 135 GPa is $\approx 4\,300\,\text{K}$ [Stixrude & Lithgow-Bertelloni, 2014]: melting is thermodynamically stable throughout the entire mantle, confirming initial state H0.

## Appendix B

# Estimation of the Dynamo Delay

With $\tau_{\text{seg}} \approx 40\,\text{Myr}$ and $\Lambda_{\text{Els}}^{\text{crit}} \approx 0.3$, the magnetic field exceeds $B_{\text{crit}} \approx 3.2\,\mu\text{T}$ at $t \approx 330\text{–}350\,\text{Myr}$ ($\approx 4.2\,\text{Ga}$). The associated uncertainty is $\pm 50\,\text{Myr}$.

## Appendix C

# Derivation of the $\lambda_{\text{global}}$ Equation

Equation (5.1) is derived from the equation of motion in the co-rotating body frame:

$$\rho\,\ddot{r} = -\rho\,g_{\text{eff}}(\varphi) + [\text{Coriolis}] + [\text{Euler}] + [\text{Maclaurin}] + [\text{Archimedes}].$$

The $\cos\varphi$ factor in $\lambda_2$ arises from the projection of the radial Coriolis force onto the local normal to the spheroid. Term $\lambda_4$ is obtained by projecting $\boldsymbol{a}_{\text{Euler}} = \dot{\boldsymbol{\Omega}} \times \boldsymbol{r}$ onto the local normal: $a_{\text{Euler}} \cdot \hat{r} = |\dot{\Omega}|\, r(\varphi)\sin(\varepsilon + \varphi)$. The amplification factor $\rho_0/\rho_{\text{TMC}}(t)$ arises naturally by setting $\delta r \propto e^{\lambda t}$.

## Appendix D

# Derivation of $\tau_{\text{Stokes}} \approx 257\,\mathbf{s}$

The Stokes settling velocity for a spherical Fe-Ni droplet in molten silicate is:

$$v_{\text{Stokes}} = \frac{2}{9}\frac{(\rho_{\text{Fe}} - \rho_{\text{sil}})\, g_{\text{eff}}^{(0)}\, r^2}{\eta} \tag{D.1}$$

with: $\rho_{\text{Fe}} \approx 7\,800\,\text{kg m}^{-3}$ [Rubie et al., 2003]; $\rho_{\text{sil}} \approx 4\,500\,\text{kg m}^{-3}$ [Rubie et al., 2015]; $\Delta\rho \approx 3\,300\,\text{kg m}^{-3}$; $g_{\text{eff}}^{(0)} \approx 6.42\,\text{m s}^{-2}$; $r \approx 5\,\text{cm}$ [Rubie et al., 2003, Solomatov, 2000]; $\eta \approx 0.1\,\text{Pa s}$ [Giordano et al., 2008]. This gives:

$$v_{\text{Stokes}} \approx \frac{2}{9} \times \frac{3\,300 \times 6.42 \times (0.05)^2}{0.1} \approx 118\,\text{m s}^{-1}. \tag{D.2}$$

Over a characteristic settling distance $\ell \approx 30\,\text{km}$:

$$\tau_{\text{Stokes}} = \frac{\ell}{v_{\text{Stokes}}} \approx \frac{3 \times 10^4}{118} \approx 257\,\text{s}. \tag{D.3}$$

This is four orders of magnitude shorter than the reloading interval ($\tau_{\text{rec}} \approx 10^6\,\text{s}$). The conclusion — chemical distinctness of successive ejection layers — is robust over the full plausible range $r \in [1; 10]\,\text{cm}$ and $\eta \in [0.05; 1]\,\text{Pa s}$.

# Appendix E

# Interactive Numerical Simulation

A WebGL/HTML5 simulation allows real-time visualization of the Triple Phase Transition dynamics: chaotic precession in the body frame, exponential growth of $U_{\mathrm{TMC}}$, progressive lightening by Fe-Ni segregation, ejection episodes from all body-frame latitudes, post-ejection transient precession, and localization of seismic interface P1. Model parameters ($\varepsilon$, $\Omega$, $\alpha$, $f_{\mathrm{cap}}$, $N$) are interactively adjustable.

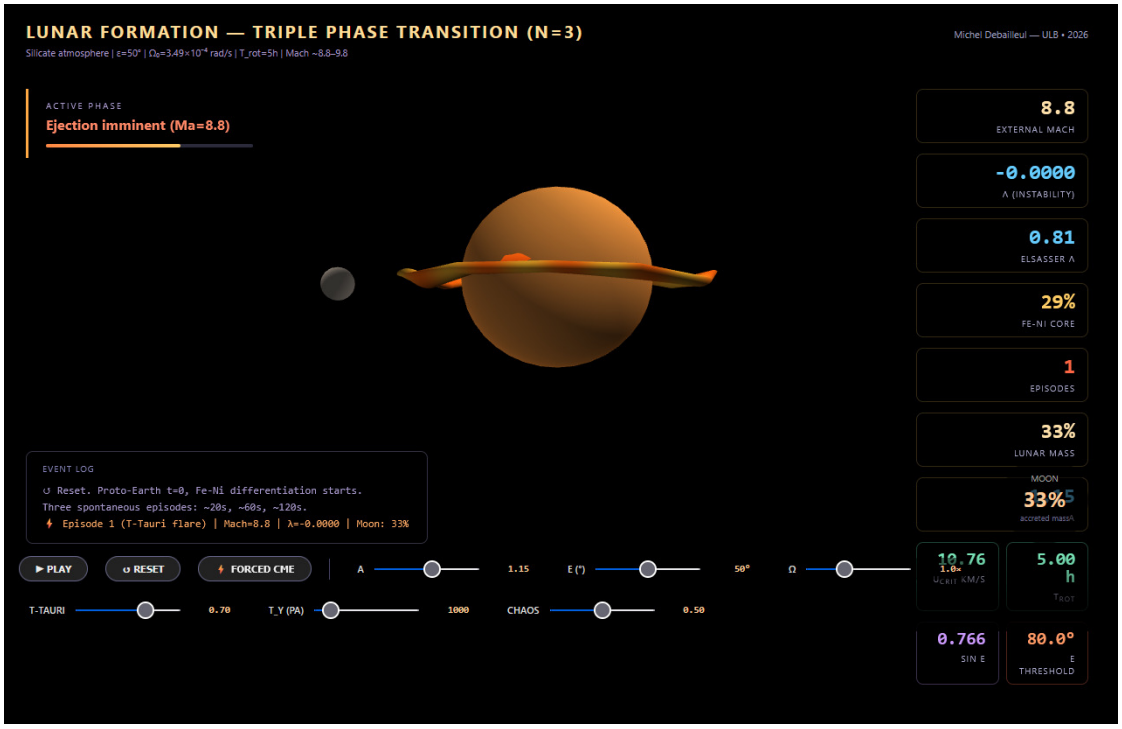


**Figure E.1:** Static screenshot of the interactive WebGL/HTML5 simulation (native WebGL, no external library). The proto-Earth (oblate Maclaurin spheroid, $T_{\mathrm{rot}} \approx 5\,\mathrm{h}$, $\varepsilon = 50°$) is shown during Episode 1 with the Coherent Magmatic Torus at Mach 8.8. Live animation: https://orion4622.github.io/moon-formation-triple-phase-transition/.

# Acknowledgments

The author thanks the anonymous reviewers for their constructive comments. This research made use of NASA's Astrophysics Data System (ADS) and the Python programming language.

# Bibliography


Agnor, C. B., Canup, R. M., & Levison, H. F. 1999, *Icarus*, 142, 219–237.

Airapetian, V. S., Glocer, A., Gronoff, G., Hébrard, É., & Danchi, W. 2016, *Nature Geoscience*, 9, 452–455.

Bingham, E. C. 1922, *Fluidity and Plasticity*. New York: McGraw-Hill.

Borg, L. E. & Carlson, R. W. 2023, *Annual Review of Earth and Planetary Sciences*, 51, 25–52.

Caricchi, L., Burlini, L., Ulmer, P., et al. 2007, *Earth and Planetary Science Letters*, 264, 402–419.

Chandrasekhar, S. 1969, *Ellipsoidal Figures of Equilibrium*. New Haven: Yale University Press.

Canup, R. M. 2004, *Icarus*, 168, 433–456.

Canup, R. M. 2012, *Science*, 338, 1052–1055.

Canup, R. M. & Asphaug, E. 2001, *Nature*, 412, 708–712.

Čuk, M. & Stewart, S. T. 2012, *Science*, 338, 1047–1052.

Dauphas, N. 2017, *Nature*, 541, 521–524.

Elkins-Tanton, L. T. 2012, *Annual Review of Earth and Planetary Sciences*, 40, 113–139.

Feigelson, E. D. & Montmerle, T. 1999, *Annual Review of Astronomy and Astrophysics*, 37, 363–408.

Garcia, R. F., Khan, A., Drilleau, M., et al. 2019, *Space Science Reviews*, 215, 50.

Giordano, D., Russell, J. K., & Dingwell, D. B. 2008, *Earth and Planetary Science Letters*, 271, 123–134.

Gowman, G., Wakita, S., Johnson, B. C., et al. 2026, *Journal of Geophysical Research: Planets*, 131, e2026JE009665.

Herschel, W. H. & Bulkley, R. 1926, *Kolloid-Zeitschrift*, 39, 291–300.

Kerswell, R. R. 2002, *Annual Review of Fluid Mechanics*, 34, 83–113.

Kleine, T., Münker, C., Mezger, K., & Palme, H. 2002, *Nature*, 418, 952–955.

Kokubo, E. & Genda, H. 2010, *Astrophysical Journal Letters*, 714, L21–L25.

Lacaze, L., Le Gal, P., & Le Dizès, S. 2004, *Journal of Fluid Mechanics*, 505, 1–22.

Laskar, J., Joutel, F., & Robutel, P. 1993a, *Nature*, 361, 615–617.

Laskar, J. & Robutel, P. 1993b, *Nature*, 361, 608–612.

Li, Q. L., Zhou, Q., Liu, Y., et al. 2021, *Nature*, 600, 54–58.

Malkus, W. V. R. 1968, *Science*, 160, 259–264.

Noir, J. & Cébron, D. 2013, *Journal of Fluid Mechanics*, 737, 412–439.

Poincaré, H. 1910, *Bulletin Astronomique*, 27, 321–356.

Rhines, P. B. 1975, *Journal of Fluid Mechanics*, 69, 417–443.

Rubie, D. C., Melosh, H. J., Reid, J. E., et al. 2003, *Earth and Planetary Science Letters*, 205, 239–255.

Rubie, D. C., Jacobson, S. A., Morbidelli, A., et al. 2015, *Icarus*, 248, 89–108.

Rufu, R., Aharonson, O. & Perets, H. B. 2017, *Nature Geoscience*, 10, 89–94.

Safronov, V. S. 1969, *Evolution of the Protoplanetary Cloud and Formation of the Earth and Planets*. Moscow: Nauka.

Schultz, P. H. & Crawford, D. A. 2011, *Geological Society of America Special Paper*, 477, doi:10.1130/2011.2477(07).

Solomatov, V. S. 2000, in *Origin of the Earth and Moon*, eds. R. M. Canup & K. Righter, Tucson: University of Arizona Press, 323–338.

Sossi, P. A., et al. 2025, *Treatise on Geochemistry*, 3rd ed., 417–479.

Stixrude, L. & Lithgow-Bertelloni, C. 2014, *Philosophical Transactions of the Royal Society A*, 372, 20130076.

Tarduno, J. A., Cottrell, R. D., Davis, W. J., et al. 2015, *Science*, 349, 521–524.

Tarduno, J. A., Cottrell, R. D., Bono, R. K., et al. 2020, *Proceedings of the National Academy of Sciences*, 117, 2309–2318.

Tarduno, J. A., Zhou, T., Huang, W., & Jodder, J. 2025, *National Science Review*, 12, nwaf082.

Touma, J. & Wisdom, J. 1993, *Science*, 259, 1294–1297.

Wakita, S., Johnson, B. C., Andrews-Hanna, J. C., et al. 2026, *Science Advances*, 12, eaea1984.

Weber, R. C., Lin, P.-Y., Garnero, E. J., Williams, Q., & Lognonné, P. 2011, *Science*, 331, 309–312.

Wieczorek, M. A., et al. 2013, *Science*, 339, 671–675.

Zuber, M. T., et al. 2013, *Science*, 339, 668–671.